

NAGW-976
IN-76-CR
167492

Structural Anomalies in Undoped Gallium Arsenide Observed in High Resolution Diffraction Imaging with Monochromatic Synchrotron Radiation

48P

B. Steiner, M. Kuriyama, R. C. Dobbyn, U. Laor^{a)}
National Bureau of Standards, Gaithersburg, MD 20899

D. Larson and M. Brown
Grumman Aerospace Corporation, Bethpage, New York 11714-3580

August 16, 1988

Novel, streak-like disruption features restricted to the plane of diffraction have recently been observed in images obtained by synchrotron radiation diffraction from undoped, semi-insulating gallium arsenide crystals. These features were identified as ensembles of very thin platelets or interfaces lying in {110} planes, and a structural model consisting of antiphase domain boundaries was proposed. We report here the other principal features observed in high resolution monochromatic synchrotron radiation diffraction images: (quasi)cellular structure; linear, very low-angle subgrain boundaries in <110> directions, and surface stripes in a <110> direction. In addition, we report systematic differences in the acceptance angle for images involving various diffraction vectors. When these observations are considered together, a unifying picture emerges. The presence of ensembles of thin {110} antiphase platelet regions or boundaries is generally consistent not only with the streak-like diffraction features but with the other features reported here as well. For the formation of such regions we propose two mechanisms, operating in parallel, that appear to be consistent with the various defect features observed by a variety of techniques.

^{a)} Present address: Nuclear Research Center, Beer Sheva, Israel

(NASA-CR-183268) STRUCTURAL ANOMALIES IN
UNDOPED GALLIUM ARSENIDE OBSERVED IN HIGH
RESOLUTION DIFFRACTION IMAGING WITH
MONOCHROMATIC SYNCHROTRON RADIATION
(National Bureau of Standards) 48 NBS-CR-183268-1

N89-11555

Unclas
0167492

PCSCI 201 G3/76

I. INTRODUCTION

Gallium arsenide is of interest in advanced approaches to high capacity information processing because: 1) the high mobility of its electrons provides substantial increase in device speed over comparable electronic circuits in silicon^{1,2,3}; and 2) successful fabrication of integrated lasers, optical and electronic signal processing elements, and detectors may lead to new generations of fast electrooptic and photonic circuits with highly parallel signal processing capability. Moreover, gallium arsenide crystals are of interest as substrates, not only for such heterojunctions, but also for infrared detectors derived from cadmium telluride, since the state of the art of substrate growth in cadmium telluride is less well advanced.

However, success with these new technologies depends on the satisfactory fabrication of large scale integrated circuits; this will be affected by the uniformity of gallium arsenide crystals, which to date is much lower than the silicon now used^{1,2,3,4,5,6,7,8,9,10,11,12,13,14,15,16,17,18,19}. For example, the incidence of electronic nonuniformities such as deep level traps^{3,11,15,20,21,22,23}, variation in the electrical properties of individual elements in integrated circuitry such as field effect transistors^{1,3,5,6-9,11-12,14-17,19}, and the quantum efficiency of injection lasers²⁴ have been shown to be correlated with the distribution of crystallographic defects, although the interpretation of the evidence may be complex^{25,26}. While the uniformity of gallium arsenide growth can be increased by doping with materials such as indium, dopants can reduce the

performance of devices not only in the vicinity of the doping sites, but at remote locations as well through dopant migration along the remaining defects. An understanding of the prevalent defect structures is thus an important step either to the direct achievement of defect-free structures or to greater effectiveness in other approaches, such as doping, to the achievement of more uniformly useful crystals.

Structural nonuniformities in undoped gallium arsenide have been observed by chemical etching^{5,10,15-16,18,26,27,28,29,30,31,32,33,34,35}, infrared absorption^{15,27,32,36,37}, photoluminescence^{6,18,24}, electron paramagnetic resonance^{21,22}, surface ionization mass spectrometry^{9,18,22,24}, electron microscopy^{31,38}, x-ray diffraction^{6,9,26,39,40,41}, and x-ray diffraction imaging (topography)^{1-2,4,18,26,28,31,33-37,42,43,44,45}. The results of these studies are highly, if not perfectly, correlated^{5,6,15,18,27-29,31-35}. The principal structural nonuniformities observed in transverse-cut [001]-grown crystals from the middle of a boule are: a cellular structure^{4,15,18,26,29,31-33,37,43-45} varying in density radially in a "W" pattern^{15,18,27,31-33,35} and azimuthally in a pattern bearing the four-fold (001) symmetry defined by the $\langle 110 \rangle$ and $\langle 100 \rangle$ directions^{2,15,26-27,33,35,43-45}; linear very low-angle (subgrain tilt) boundaries also arrayed in the four-fold symmetry associated with the $\langle 110 \rangle$ directions in the (001)-cut surface^{26,28,35-37,44-45}; variation in "strain field"^{6,9,39-41} with a four-fold symmetry (with eight maxima for low-defect-density crystals)^{1,2,28}; variation in lattice orientation in a two-fold⁴³⁻⁴⁵ or four-fold pattern²⁸ associated with $\langle 110 \rangle$ directions in the (001) surface; and a much smaller variation in lattice parameter⁴⁰ in a two-fold or four-fold pattern^{28,43}.

The firm identification of the defect structure(s) responsible for these variations, which are characterized by similar symmetry, has proved elusive, however^{29,31}. The impurity level in such material is typically too low for impurities to be completely responsible for the observed anomalies^{9,18,26}. The close correlation of etch pit density with the cellular structure seen in topography has led to the association of etch pits with dislocations^{15,18,33-35,37,46} but the typical variation in the visibility of individual dislocation strain features with diffraction vector orientation has not been observed^{4,31,45}.

High resolution diffraction imaging with monochromatic synchrotron radiation provides a sensitive tool for study of the genesis, distribution, and characteristics of such crystallographic imperfections^{47,48}. At the sub-arc-second angular resolution now available, x-ray diffraction images indicate the presence, structure, and orientation of individual crystal defect features not previously observed in images with an area of several square centimeters, large enough to show levels of incidence and precise spatial relationships. This information is complemented by that provided by electron microscopy, which is capable of much higher spatial resolution, but lower angular resolution over much smaller areas. The new x-ray information can be used to analyze the various types of defect, to evaluate the prevalence, and to guide the manipulation of individual growth parameters⁴⁹ in order to control their formation.

The large storage ring at the National Synchrotron Light Source (NSLS) provides the brightest and smallest optical source available for such imag-

ing. These characteristics are important because they provide for maximum information from unthinned samples, and for maximum strain sensitivity and useful spatial resolution, respectively. The diffraction imaging beam line (X23-A) at NSLS on which this work was carried out was designed and developed by the National Bureau of Standards to augment these key characteristics through utilization of asymmetrically-cut, large, flat monochromator crystals^{47-48,50}. This optical arrangement simultaneously expands the size of the available beam and decreases its divergence, providing angular resolution to 0.4 arc-second over an area of several square cms. Observations are made both with high spatial resolution (1 μm) and with real-time intermediate spatial resolution (30 μm).

With the new resolution thus made available, we have observed several (001)-cut undoped, semi-insulating gallium arsenide crystals from various sources. The imperfection images have the general character of lower resolution images^{1-2,4,18,26,28,33-35,37,43-45}, which indicates that these crystals are typical of high quality gallium arsenide crystals. At the same time, new features are also observed at high resolution. Quantitative comparison of the various features in these images indicates, moreover, that they are interrelated. The new detail visible at the high resolution of the current experiments suggests that antiphase boundaries are pervasive. A simple antiphase boundary model of the defect structure appears to explain all the principal features observed in gallium arsenide and is consistent with similar features in the diffraction imaging of cadmium telluride as well.

II. EXPERIMENTS PERFORMED

Four samples of undoped gallium arsenide grown by liquid encapsulated Czochralski techniques in various laboratories have been examined in Bragg (reflection) geometry, and two of these in Laue (transmission) geometry as well. These crystals, each between 500 and 600 μm thick, had been well polished so that no visible surface features remained. One of these, sample GaAs 5, had been cut to approximately 8 mm square; while the other, sample GaAs 4, was taken from the periphery of a 4 inch (10 cm) boule cut to include the edge and two straight orthogonal (110) planes approximately three and four cm long, respectively.

Sample GaAs 5 was of sufficiently high quality that the entire sample could be studied simultaneously with the large area ($\sim 10\text{cm}^2$), high resolution beam formed by our flat crystal monochromator in its magnification configuration. Monochromator magnification by two different factors, 4 and 100, was employed, which provides beams of 2 and 0.4 arc-second (10^{-5} and 2×10^{-6} radians) divergence, respectively. With these beams, we observed (004) and ($\bar{4}$ 44) diffraction images in Bragg geometry, and (400) and ($2\bar{2}$ 0) diffraction images in Laue geometry with eight and ten KeV photon energy.

Sample GaAs 4 was studied in Bragg geometry also with a monochromator magnification factor of four (2 arc-second, or 10^{-5} radian, divergence), with which both (004) and ($\bar{4}$ 44) diffraction images were observed. For this crystal, diffraction in Laue geometry was carried out with the monochro-

mator in both factor-of-four magnification and demagnification modes, the latter illuminating a smaller fraction of the crystal with lower (8 arc-second, or 4×10^{-5} radians) angular resolution. With these beams, (040) and (220) diffraction images were observed.

Independent of the variation in beam energy and in beam divergence utilized in the various experiments, corresponding images for the crystals are qualitatively similar to each other and to earlier work^{1-2,4,18,26,28,33-35,37,43-45}. However, the new results display detail not previously in the general features commonly believed to be typical of such material.

III. THE DIFFRACTION IMAGES

A. Principal Features

Pervasive streak-like disruption features aligned with the direction of diffraction in Laue geometry were reported for the first time recently^{4,2}, and are evident diagonally in Figure 1 and vertically in Figure 2. The two principal types of feature characteristic of topography at lower resolution are evident in high resolution as well. One of these is a pronounced cellular structure^{4,15,18,33,37,43-45} distinguished by irregular boundaries and, in some regions of these images, by very small differences in lattice orientation, as observed by Kitano, Matsui, and coworkers⁴⁴⁻⁴⁵. This structure is striking in Figures 2-4, taken in Bragg geometry, as well

as in Figure 5, taken Laue geometry. In contrast to work at lower resolution³, however, important differences among images observed under different diffraction conditions become pronounced at high resolution.

The second type of general feature is linear low-angle subgrain boundaries, evident in Bragg geometry as a vertical demarcation between areas of sharp contrast, Figures 6 and 7, and in Laue geometry as a vertical poorly diffracting stripe 50 μm wide in Figure 8. Such boundaries have been observed in lower resolution in laboratory topography^{26,28,35,44-45} and at the Daresbury and Tsukuba synchrotrons,^{36-37,45}

Observations of these samples in Bragg geometry are characterized also by systematic differences in acceptance angle: the ($\bar{4}44$) diffraction images (Figures 4 and 9) appear over a broader incident angle range than do the (004) diffraction images of the same samples (Figures 6 and 10). Observation of such differences, of course, requires a relatively small incident beam divergence, much less than the acceptance angle (or the theoretical rocking curve width).. For the (004) diffraction images, which appear over a relatively small acceptance angle (~ 12 arc-seconds), variation in strain over the surface of the crystals can be estimated to be similar in character to that previously observed^{1,9,40-41,43,45}.

A third type of feature, sets of linear surface stripes, is prominent in images of sample GaAs 5 but not in the others. These stripes are clearly seen horizontally across the bottom of Figure 11, taken in Bragg geometry, and Figures 12 and 13, taken in Laue geometry. These features

may have been caused by surface treatment rather than the initial growth of the crystal, but they are not visible under an optical microscope in visible light. Moreover, the structure of these features appears to fit into the general antiphase boundary interpretation of the structure of undoped gallium arsenide that follows from an analysis of the other principal aspects of these high resolution images.

B. Streak-like Features

Pervasive streak-like features oriented along the diffraction vector, such as those in Figures 1 and 2, are evident in all high resolution diffraction images taken of gallium arsenide in Laue geometry⁴², of which Figures 12 - 13 are typical in this respect. Individual streak-like features extending in the direction of diffraction in a given image are found only in images with that diffraction vector and are distinct from similar features extending in other directions visible only in other images of the same region of a given crystal. For example, the streak-like features oriented in the direction of diffraction in $(2\bar{2}0)$ images are not seen in (400) or $(0\bar{4}0)$ images, while the features oriented in the direction of diffraction in one of the latter images are not observed in $(2\bar{2}0)$ images.

The clear observation of such closely spaced features principally as disruption of diffraction in Laue geometry, their appearance identically in H and O pairs of images for a particular diffraction, and their absence in

images in Bragg geometry all indicate that such anomalies in the structure of gallium arsenide are pervasive in the crystal interior. The observation of a given set of streak-like features only in a particular diffraction orientation can be interpreted only in terms of very thin platelet or interfacial structures that are coherent with the crystal matrix but displaced from it⁴². Where such unique coherence of intrusive structures with the adjacent lattice is not preserved (as is the usual case for imperfections) or where a mutual displacement of the lattices is not present, visibility of the region in diffraction varies as a function of the cosine of the angle between the diffraction vector and the local atomic displacement, (for example, the Burgers vector for dislocations). Such visibility changes much more slowly with angle than does the discrete visibility of the platelets in gallium arsenide crystals observed in high resolution diffraction imaging in Laue geometry.

The width and orientation of these features in the various images indicate that they are due to (110) platelets with a thickness less than the one μm resolution limit of the present observations⁴². The more isolated platelets or interfaces appear to extend 200 - 300 μm parallel to the surface of the crystal in the direction of diffraction and 50 μm in an orthogonal direction oblique to the surface, the particular angle depending on the particular (110) orientation of the platelet or interface. (Shown in Figure 14, Feature A.) Other platelets are rotated in their plane by 90° and are associated with the cellular structure. (Shown in Figure 14, Feature B.)

C. Cellular Structure

The cellular structure previously reported at low resolution-4, 15, 18, 33, 37, 43-45 is visible in all of the Figures, but is especially prominent in Figures 2 - 5. With the resolution of the current experiments, however, previously unresolved fine structure in many of the cell "boundaries" is detected. This fine structure varies from image to image. While there is a correlation in the location of some of the cell-like features in the various images of a given crystal region (as reported at lower resolution in observations in Lang topography⁴), the distribution and orientation of many of the cell-like features differ from diffraction image to diffraction image at the resolution of these experiments. For example, the structure in the (400) H beam image of crystal GaAs 5, Figure 1, differs from the structure in the (2 $\bar{2}$ 0) H beam image of the same region of the same crystal shown in Figure 1 of Reference 42. This variation in visibility of the structure of the cell-like images with diffraction is similar to the variation with diffraction of the streak-like images of the isolated platelets. Indeed, many of the boundary regions appear to be constructed of platelets similar in general character to those that make up the more isolated streak-like features.

Those platelets embedded in or constituting the boundaries, however, appear to be lined up like dominos arranged face-to-face (Figure 14, Feature B). They appear to differ also from the isolated platelets (Figure 14, Feature A) in their orientation. Thus, not only are the boundary

platelets arrayed face-to-face, but they appear to be rotated in their plane ninety degrees with respect to the isolated platelets in the interior of the cells. The platelets forming the cell walls appear to be oriented with their 50 μm width parallel to the surface of the crystal in the direction of diffraction. The result is that the boundary region images have a characteristic width of 50 μm . There are some wider boundary regions as well, but they may be composed of two or more 50 μm platelets arranged in line. Some boundary regions consist of individual lines rather than platelets.

D. Near Linear, Very Low-Angle Subgrain Boundaries

Linear very low-angle (2-20 arc-seconds) subgrain boundaries similar to those previously reported^{26,28,35-37,44-45} are prominent vertically in Figures 6 and 7 in Bragg geometry and in Figure 8 in Laue geometry. These boundaries observed all lie in {110} planes at near right angles to the (001) surface. In Bragg geometry, shown in magnification in Figure 11, the intersection of such a boundary with the surface of the crystal appears as a vertical discontinuous line at the left side of the Figure. This feature has a width (1 μm) limited by the resolution of the nuclear emulsion plates. In Laue geometry, however, the width of the entire boundary region in the interior of the crystal is seen to be greater, 50 μm , observed in Figures 12 - 13 as a vertical stripe along the left hand edge.

Under observation by video camera as a crystal is rocked in the vicinity of the diffraction peak, the variation in contrast across such bound-

aries indicates that the difference in orientation of the crystal lattice on opposite sides of the boundaries ranges from 2 to 20 arc-seconds around an axis of rotation defined by the intersection of the observed (110) boundary and the (001) surface of the crystal. Misorientation orthogonal to this, that is, around an axis in the surface of the crystal perpendicular to the principal misorientation axis, was not detected and, therefore, is negligible by comparison in all such crystals studied, as was observed also by Barnett, Brown, and co-workers³⁶⁻³⁷. The misorientation observed is comparable to the misorientation reported for similar boundaries in other crystals of gallium arsenide crystals^{26,37,45}. In complete slices from a given boule, these boundaries are observed to form a pinwheel configuration in a wafer cut orthogonal to the growth direction²⁶.

E. Acceptance Angle Differences among the Diffraction Images

Another characteristic aspect of all undoped gallium arsenide images observed in high resolution is a large systematic variation in the acceptance (sample crystal rocking) angles for the various images. The ($\bar{4}44$) images appear over an acceptance angle wider by about a factor of three than the acceptance angle for the (004) images which is 12 arc-seconds. As a result of this spread, the contrast of the features in ($\bar{4}44$) images (Figures 4 and 9) is observed to be substantially lower than is the contrast in the corresponding (004) images (Figures 6 and 10). This variation in acceptance angle with diffraction vector indicates that the local lattice parameter varies more inhomogeneously in $\langle 111 \rangle$ directions than in $\langle 100 \rangle$ and

$\langle 100 \rangle$ directions. Such broadening due to local atomic displacements depends on the angle between the lattice displacement and the diffraction vectors.

F. Surface Stripes

In contrast to the preceding characteristics, which are shared by all of the high resolution images, one feature is prominent in the images of only one of the crystals. Figures 11 - 13 display sets of striped features that are of the order of $50 \mu\text{m}$ width and several mm in length along the $[110]$ direction.

The stripes observed in the Bragg images, such as Figure 11, are roughly symmetric about a plane between the stripes. The stripes in the pairs taken in Laue geometry are unusual in that the contrast in the stripes in the H image (Figure 12) is reversed from the contrast in the corresponding 0 image (Figure 13). That is to say, those regions made visible by disruption of transmission bounded by regions of high transmission are seen in the other image of the pair in Laue geometry as regions of high transmission bounded by regions of disrupted transmission. Such contrast reversal is observed typically in small areas of an image recorded in Laue geometry where a crystal anomaly such as a scratch is located at the x-ray exit surface⁵¹. Correlated contrast changes in the images of such surface features are observed in Bragg geometry as the crystal is rocked in the vicinity of the Bragg peak. These changes arise from interference between kinematical and dynamical scattering near the surface of

the crystal. However, the observation of uniform contrast reversal over such substantial crystallographically oriented regions represented by these stripes, 50 μm wide and several mm long, is unusual. Both the visibility of the stripes in Bragg geometry and their contrast reversal in the Laue geometry image pairs clearly indicate that these features are close to the (x-ray exit) surface of the crystal.

The symmetry of the Bragg images and the alternation of diffraction in the Laue image pairs suggests surface misorientation (or uniform atomic displacement) of the lattice within a 50 μm stripe bounded by $(\bar{1}10)$ planes, leading to diffraction alternately in the two directions, H and O, in successive stripes⁵¹.

IV. STRUCTURAL SOURCE OF THE FEATURES OBSERVED

These seemingly unrelated features are characterized by a small number of identical parameters. The platelets (both those on the cell boundaries and those arrayed in the interior of cells) are oriented in (110) planes, as are the linear low-angle grain boundaries and the edges of the surface stripes. The cell wall platelets, the cell interior platelets, the low-angle grain boundary structure in the interior of the crystal, and the surface stripes are all approximately 50 μm wide. The difference in lattice orientation across a number of the irregular cellular boundaries as well as on opposite sides of many of the linear low-angle grain boundaries is of

the order of two arc-seconds, although the latter may extend to twenty arc-seconds.

These characteristic parameters can be related to one another through a very low-angle (110) lattice tilt boundary. If we postulate a region of the gallium arsenide crystal lattice tilted with respect to the adjacent lattice by two arc-seconds (the macroscopic tilt observed across some adjacent cell boundaries and across some linear subgrain boundaries), the lattice on the two sides of such an interface will regain registry in 50 μm , (shown in Figure 15) which is the characteristic width of the platelets, the characteristic width of the boundaries of many of the cells, the width of the linear very low-angle subgrain boundary region in the interior of the crystal, and the width of the surface stripes. This tilt is associated with a series of inhomogeneous minute atomic displacements propagating throughout the boundary interface, resulting in a lattice shift of one unit cell in the $\langle 110 \rangle$ direction (normal to the boundary) after 50 μm , as shown in Figure 15. These boundaries may be grouped in two ways. When they appear face-to-face, they create a tilt angle larger than two arc-seconds (shown in Figure 16). When such groups are aligned end-to-end, linear (110) very low-angle subgrain boundaries form with a tilt angle ranging from 2 to 20 arc-seconds (shown in Figure 14).

Such two arc-second very low-angle (110) subgrain boundary structures, associated with a coherent lattice shift and the propagation of minute atomic displacements throughout the boundary, appears to be consistent with all of the principal features in the images: the cell boundaries, the

near-linear macroscopically observed very low-angle subgrain boundaries, the isolated platelets responsible for the streak-like images, and the surface stripes.

What structural anomalies are consistent with the size, orientation, and distribution of these features and will interact with x-rays in the manner observed in these high resolution images? Stacking faults, twins, and slip planes are expected to form images lying in (111) planes; and this orientation should be evident in a manner corresponding to the identification of the anomalous features actually observed in (110) planes, if they are coherent with the lattice and displaced from it, or otherwise by the conventional cosine-type "strain visibility". Isolated dislocations cannot appear in diffraction images only when the diffraction vector is perpendicular to a specific direction, say, $\langle 110 \rangle$. Rather, they are expected to exhibit a cosine dependence in the visibility with angle, which would permit the determination of the direction of the associated Burgers vector^{4, 31, 45}. Neither behavior, associated with (111) planes, is observed. There is no basis for restriction of the visibility of large precipitates or voids to images along the diffraction vector perpendicular to $\langle 110 \rangle$ directions.

The fact that pervasive structural anomalies are observed in gallium arsenide and perhaps in other III-V and II-VI crystals, but not in the best Group IV crystals, suggests that the anomalies are associated with the presence of sublattices of dissimilar atoms, because the atoms occupy the same basic positions in the unit cell. In contrast to other defects,

antiphase boundaries in gallium arsenide, after being nucleated during crystal growth through interchange of gallium and arsenic, must propagate along {110} planes, which contain bonded nearest neighbors. These {110} boundaries will retain lattice coherence across the boundary, but be marked by a lattice displacement because of the anomalous bonding between like atoms at the interface, in contrast to the interior of a domain. These are the characteristics of the sources of the streak-like features observed in high resolution diffraction images. The observed distinct visibility condition closely associated with a diffraction vector, unlike the visibility/invisibility condition for isolated strains, is consistent either with an infinitesimally thin, single antiphase boundary or with a complete antiphase region with thickness less than one μm . Since the two sublattices are distinguishable in III-V and II-VI crystals, they would be expected in such crystals but not in silicon and germanium, in which similar pervasive features are indeed not observed.

Thus, of the various defects--stacking faults, twins, slip planes, isolated dislocations, precipitates, voids, and antiphase boundaries--only antiphase boundaries are consistent with the observation of structural anomalies restricted to {110} planes and maintaining lattice coherence, but with a lattice displacement.

Such boundaries, at least in many cases, appear to propagate with a 2 arc-second tilt for about 50 μm , at which point lattice match is again obtained and propagation ceases (shown in Figure 15). Where a row of atoms normal to the bulk growth direction simultaneously nucleates such a

boundary, the lattice tilt is oriented in the direction of growth (Type A in Figures 14 and 15). The anomaly propagates for 50 μm in that direction, at which point lattice match is regained and the propagation of the antiphase region is aborted. In such instances, the antiphase regions are relatively isolated, as observed of the streak-like features in the interior of the cell-like structural anomalies. Where a single atom occupies an antisite and initiates a row of antiphase atoms in the $\langle 001 \rangle$ bulk growth direction, the resulting lattice tilt angle orientation and associated 50 μm propagation limit are normal to the direction of propagation (Type B, Figures 14 and 15). In this case, adjacent, face-to-face platelets appear to be initiated about the same time, forming a domino-like array, 50 μm wide, observed as a "cellular" boundary (shown in Figure 14).

Where an extended $\langle 110 \rangle$ row of antisite atoms forms normal to the growth direction, a linear low-angle subgrain boundary may be initiated to form a (110) plane, either (1) as an isolated platelet or interface (Type A, Figures 14 and 15), (2) as a linear, very low-angle subgrain boundary (Type C, Figure 14), or (3), if near the surface, a set of surface stripes (perhaps coalescing as a result of subsequent surface treatment). The restriction of the stripes to a surface region and their observations in only one of the samples suggest that they may not be growth related. Nevertheless, the similarities in the characteristic parameters that describe them to the parameters of the other anomalies strongly implies that the stripes represent aggregate antiphase regions.

Antiphase boundaries would be expected to react to chemical etching in a manner similar to, but perhaps distinguishable from, that of isolated dislocations whether or not dislocations form part of their structure (i.e. whether or not a tilt is associated with the interface)^{30,32,52}. The presence of such boundaries thus appears to be consistent with etch pit experiments^{5,15-16,18,26-35}, and especially with the distinction shown between cell walls and other regions,²⁹ with infrared absorption^{15,27,29,31,36-37}, with electron microscopy, in which lattice coherence is determined but in which Burgers vectors cannot be determined^{29,31} with the x-ray diffraction evidence for lattice strain (with allowance for lattice tilt)^{6,9,11,39-41,43-45}, with observations made with bulk electrical measurements, with other {110} anomalies observed in topography², and with the observation of the influence of thermal factors during growth^{35,53}. Moreover, such boundaries would frustrate attempts to determine Burgers vectors from electron micrographs and from topographs, as has been noted^{5,29,31,45}, in spite of the ability to do so for <111>-grown undoped indium phosphide⁵⁴. The streak-like interface images will appear at precisely the orientation at which any associated edge dislocation becomes invisible. The difference in etch pits between those associated with native defects and those associated with deformation-induced dislocations, as observed²⁴, is also understandable in light of an antiphase model for native defects. Antiphase domains have been postulated in cadmium telluride and related films, which have the same crystal structure⁵⁵.

More specifically, the prevalence of antiphase regions is consistent with the postulated antisite origin of EL2 defects^{21,22,56,57,58,59,60}, and

related observations on the influence of arsenic stoichiometry on the incidence of anomalies^{10,21,61,62,63}. The antiphase model is particularly consistent with the arsenic cluster antisite model^{20,56}, with the platelet form proposed for the infrared-active regions¹⁵, and with the 50 μm region of anomalous electrical behavior that has been observed^{5,16,24}. The presence of various ensembles of antiphase boundaries thus appear to be consistent with all defect observations and with antisite models for bulk infrared activity, while models for other types of defects appear to be inconsistent with one or more of the various observations. Moreover, the antiphase model for defects provides insight into why Bridgman-grown gallium arsenide crystals are most perfect when seeded in the $\langle 013 \rangle$ direction⁶⁴.

V. ANTIPHASE BOUNDARY NUCLEATION MECHANISMS

We do not yet have sufficient information to determine the size or the direction of the displacement observed at the antiphase boundary. We can ask, however, how such antiphase boundaries might be nucleated. Development of an antiphase boundary in a propagating surface requires the establishment of an antiphase $\langle 110 \rangle$ row of atoms bound laterally to like atoms, in place of the lower energy binding to dissimilar atoms. Calculations of the energy of formation of (001) surfaces⁶⁵, confirmed by recent observation of epitaxially growing, "reconstructed" gallium arsenide surfaces by scanning tunneling microscopy⁶⁶, provide one mechanism for such a nucleation step, where the nucleating row is normal to the growth axis. For a

growing arsenic (001) plane, the filling of every fourth or eighth row on a "reconstructed" surface proves to be less energetically favorable than the filling of the other rows. During orderly growth, therefore, these higher energy rows will fill last. Initiation of the growth of a (001) gallium layer before completion of the preceding (001) arsenic layer will provide the opportunity for establishment of just such a row of homopolar bonds as required for the nucleation of an antiphase boundary. Two parallel (110) interfaces, aligned with the growth direction, would thus be established, leading to formation of a (110) platelet, if the propagation conditions are suitable. After these interfaces propagate for 50 μm lattice match apparently will be regained and the propagation terminated. The local atomic displacements from the ideal lattice in this region are estimated to be of the order of 10^{-6}nm , in agreement with previous measurements of lattice parameter variation^{6,9}, and requires precision measurements locally. In this manner, isolated platelets, (Type A, Figures 14 and 15) longer low-angle subgrain boundaries, (Type C, Figure 14) and the surface striped regions apparently could be nucleated to form the various features observed in the images.

In contrast to the nucleation of an extended row of antisite occupation, if occupation of single antisite propagates during growth, an antiphase platelet rotated ninety degrees in its plane (i.e. with the propagating misorientation normal to the growth direction) may be formed in a similar manner (Type B, Figures 14 and 15). In this case, the images indicate that parallel adjacent platelets will be formed at the same time,

together marking a "cell boundary". The tilt at the interfaces may accumulate to give curvature to the "boundaries".

In either case, the homopolar bonds at the phase boundary, lying in $\langle 111 \rangle$ directions, will differ in length and direction from the length of gallium-arsenic bonds of the perfect structure, resulting in a coherent shift and lattice modulation. The magnitude of this modulation (10^{-6} nm) and the 2 arc-second tilt result in the broadening of the acceptance angle for the $(\bar{4}44)$ diffraction, as observed.

Acknowledgements

The authors acknowledge the support of the U. S. Department of Commerce and of the National Aeronautics and Space Administration, through the Center for the Development of Commercial Crystal Growth in Space at Clarkson University. The NBS Materials Science synchrotron radiation beam line is located at the National Synchrotron Light Source, Brookhaven National Laboratory, which is supported by the U. S. Department of Energy, Division of Materials Science (DOE contract number DE-AC02-76-CH00016).

FIGURES

1. Image of (400) H beam 10 keV synchrotron radiation diffracted from central portion of crystal GaAs 5 in Laue geometry. The streak-like features were first reported recently^{4,2} for the 0 beam image from this crystal, which is very similar. Those features that differ in 0 and H beam images indicate structural anomalies close enough to the surface to scatter kinematically as well as dynamically^{5,1}. This is a negative image; that is, regions of the crystal that appear dark in this image diffract more efficiently than regions that appear light.
2. Image of (0 $\bar{4}$ 0) 0 beam 10 keV synchrotron radiation diffracted from central portion of crystal GaAs 4 in Laue geometry. The streak-like features in this image are generally similar to elements in images of crystal GaAs 5 such as Figure 1. This is a negative image.
3. Cellular structure in enlarged portion of (004) diffraction from crystal GaAs 4 in 8 keV synchrotron radiation in Bragg geometry. This is a positive image; that is, regions of the crystal that appear light diffract more efficiently than regions that appear dark.
4. Image of ($\bar{4}$ 44) diffraction of 8 keV synchrotron radiation from crystal GaAs 4 in Bragg geometry. The cellular structure is particularly distinct. This is a positive image.

5. Image of $(\bar{2}\bar{2}0)$ H beam diffraction of 10 keV synchrotron radiation transmitted by crystal GaAs 4 in Laue geometry, in which cellular structure is distinct. This is a positive image.

6. Image of (004) diffraction of 8 keV synchrotron radiation from crystal GaAs 4 in Bragg geometry showing a very low-angle $\langle\bar{1}10\rangle$ subgrain boundary, marked by sharp contrast, running vertically in the figure. The acceptance angle for this diffraction is much smaller than for the $(\bar{4}44)$ diffraction for this crystal, shown in Figure 4, resulting in reduced contrast in this asymmetric diffraction. This is a positive image.

7. Image of (004) diffraction of 8 keV 0.4 arc-second synchrotron radiation from crystal GaAs 5 in Bragg geometry. The crystal has been rotated in the beam so that the $\langle 010\rangle$ direction lies in the plane of diffraction. In this orientation and with this resolution, a very low-angle subgrain boundary is observed in the $\langle\bar{1}10\rangle$ (vertical) direction, but the cellular structure is less distinct. This is a positive image.

8. Image of $(\bar{2}\bar{2}0)$ H beam diffraction of 10 keV 0.4 arc-second synchrotron radiation transmitted by crystal GaAs 5 in Laue geometry, in which cellular structure is distinct. A very low-angle $\langle\bar{1}10\rangle$ subgrain boundary, running vertically, is well-defined, as are surface $\langle 110\rangle$ stripes, running horizontally. This is a positive image.

9. Image of $(\bar{4}44)$ diffraction of 8 keV synchrotron radiation from crystal GaAs 5 in Bragg geometry. The acceptance angle for this diffraction is much larger than for the (004) diffraction from the same crystal, shown in Figures 7 and 10, resulting in reduced contrast in this asymmetric diffraction. This is a positive image.
10. Image of (004) diffraction of 10 keV 2 arc-second synchrotron radiation from crystal GaAs 5 in Bragg geometry. The crystal is oriented so that the $\langle 1\bar{1}0 \rangle$ direction lies in the plane of diffraction. The quasicellular structure is relatively visible in this image, which is positive.
11. Enlarged portion of Figure 4 showing horizontal striped features on the surface of crystal GaAs 5 observed in (004) diffraction of 8 keV synchrotron radiation in Bragg geometry. This is a negative image.
12. Enlarged portion of $(2\bar{2}0)$ H beam diffraction of 10 keV synchrotron radiation of crystal GaAs 5 in Laue geometry, showing a very low-angle subgrain boundary, running vertically, as well as $\langle 110 \rangle$ surface stripes, running horizontally. This is a negative image.
13. Enlarged portion of $(2\bar{2}0)$ O beam diffraction of 10 keV synchrotron radiation of crystal GaAs 5 in Laue geometry, showing a very low-angle subgrain boundary, running vertically, as well as $\langle 110 \rangle$ surface stripes, running horizontally. The contrast in the striped features

is seen to be inverted from that in the H beam diffraction shown in Figure 12. This is a negative image.

14. Schematic diagram of single cell, consisting of relatively isolated {110} platelets (A), 200-300 μm long (dimension in the plane of the figure) and 50 μm wide (dimension normal to the plane of the figure), and cell boundary platelets (B), whose 50 μm width is oriented in the plane of this figure. Adjacent very-low angle grain boundary (C) is also indicated.

15. Schematic diagram of interface structure consistent with observed 50 μm characteristic platelet dimension and with observed tilt of lattice between some adjacent cells and tilt of linear very low-angle grain boundary. In contrast with conventional tilt boundaries characterized by periodic arrays of dislocations, propagation of such a boundary apparently ceases at the misregistration. "Types A and B" refer to two types of platelet indicated schematically in Figure 14.

16. Schematic diagram of 2 arc-second platelets grouped to produce the observed 20 arc-second very low-angle subgrain boundary (shown in Figure 14, C).

REFERENCES

1. T. Kitano, T. Ishikawa, H. Ono, and J. Matsui, Jap. J. Appl. Phys. 25, L530 (1986)
2. T. Kitano, T. Ishikawa, H. Ono, and J. Matsui, Semi-Insulating III-V Materials, Hakone, 91 (1986)
3. J. V. DiLorenzo, A. S. Jordan, A. R. VonNeida, and P. O'Connor, Semi-Insulating III-V Materials, Kah-nee-ta, 308 (1984)
4. E. Zielińska-Rohozińska, J. Crystal Growth 87, 154 (1988)
5. S. Miyazawa, Semi-Insulating III-V Materials, Hakone, 3 (1986)
6. Y. Takano, T. Ishiba, Y. Fujisaki, and J. Nakagawa, and T. Fukuda, Semi-Insulating III-V Materials, Hakone, 169 (1986)
7. S. Miyazawa and K. Wada, Appl. Phys. Lett. 48, 905 (1986)
8. T. Sato, K. Terashima, H. Emori, S. Ozawa, M. Nakajima, T. Fukuda, and K. Ishida, Jap. J. Appl. Phys. 24, L488 (1985)
9. Y. Takano, T. Ishiba, N. Matsunaga, and N. Hashimoto, Jap. J. Appl. Phys. 24, L239 (1985)
10. J. Lagowski, H. C. Gatos, T. Aoyama, and D. G. Lin, Semi-Insulating III-V Materials, Kah-nee-ta, 60 (1984)
11. M. S. Skolnick, M. R. Brozel, L. J. Reek, I. Grant, D. J. Stirland, and R. M. Ware, J. Elect. Mat. 13, 107 (1984)
12. H. V. Winston, A. T. Hunter, H. M. Olsen, R. P. Bryan, and R. E. Lee, Appl. Phys. Lett. 45, 447 (1984)
13. S. Miyazawa and Y. Ishii, IEEE Trans. Elect. Devices ED-31, 1057 (1984)
14. Y. Ishii, S. Miyazawa, and S. Ishida, IEEE Trans. Elect. ED-31, 800 (1984)
15. M. R. Brozel, I. Grant, R. M. Ware, D. J. Stirland, and M. S. Skolnick, J. Appl. Phys. 56, 1109 (1984)
16. S. Miyazawa, Y. Ishii, S. Ishida, and Y. Nanishi, Appl Phys. Lett. 43, 853 (1983)
17. T. Honda, Y. Ishii, S. Miyazawa, H. Yamazaki, and Y. Nanishi, Jap. J. Appl. Phys. 22, L270 (1983)
18. T. Kamejima, F. Shimura, Y. Matsumoto, H. Watanabe, and J. Matsui, Jap. J. Appl. Phys. 21, L721 (1982)

19. Y. Nanishi, S. Ishida, T. Honda, H. Yamazaki, and S. Miyazawa, Jap. J. Appl. Phys. 21, L335 (1982)
20. H. J. von Bardeleben, D. Stievenard, J. C. Bourgoin, and A. Huber, Semi-Insulating III-V Materials, Hakone, 355 (1986)
21. S. Makram-Ebeid, P. Langlade, and G. M. Martin, Semi-Insulating III-V Materials, Kah-nee-ta, 184 (1984)
22. K. R. Elliott, R. T. Chen, S. G. Greenbaum, and R. J. Wagner, Kah-nee-ta, 239 (1984)
23. M. R. Brozel, I. Grant, R. M. Ware, and D. J. Stirland, Appl. Phys. Lett. 42, 610 (1983)
24. W. Heinke and J. J. Queisser, Phys. Rev. Letters 33, 1082 (1974)
25. K. Ishida, A. Yahata, and T. Kikuta, Jap. J. Appl. Phys. 24, L250 (1985)
26. P. Dobrilla, J. S. Blakemore, A. J. McCamant, K. R. Gleason, and R. Y. Koyama, Appl. Phys. Lett. 47, 602 (1985)
27. H. Kuwamoto and D. E. Holmes, private communication
28. S. J. Barnett, G. T. Brown, and B. K. Tanner, Microsc. Semicond. Materials, Oxford, 1987, in Inst. Phys. Conf. Ser 87, 615 (1987)
29. D. J. Stirland, Semi-Insulating III-V Materials, Hakone, 81 (1986)
30. H. Lessoff, Materials Lett. 3 251 (1985)
31. F. A. Ponce, F-C. Wang, and R. Hiskes, Semi-Insulating III-V Materials, Kah-nee-ta, 68 (1984)
32. D. J. Stirland, I. Grant, M. R. Brozel, and R. M. Ware Inst. Physics Conf. Ser 67 285 (1983)
33. J. Angilello, R. M. Potemski, and G. R. Woolhouse, J. Appl. Phys. 46, 2315, (1975)
34. A. G. Elliot, C. L. Wei, R. Farraro, G. Woolhouse, M. Scott, and R. Hiskes, J. Cryst. Growth 70, 169 (1984)
35. R. T. Chen, and D. E. Holmes, J. Crystal Growth 61, 111 (1983)
36. S. J. Barnett, B. K. Tanner, and G. T. Brown, Materials Research Soc. Proc. 41, 83 (1988)
37. G. T. Brown, M. S. Skolnick, G. R. Jones, B. K. Tanner, and S. J. Barnett, Semi-Insulating III-V Materials: Kah-nee-ta, 76 (1984)

38. A. G. Cullis, P. D. Augustus, and D. J. Stirland, J. Appl. Phys. 51, 2556 (1980)
39. M. Nakajima, R. Sato, T. Inada, R. Fukuda, and K. Ishida, Semi-Insulating III-V Materials: Hakone 181 (1986)
40. Y. Okada, Y. Tokumaru and Y. Kadota, Appl. Phys. Lett. 48, 975 (1986)
41. H. Kuwamoto and D. E. Holmes, J. Appl. Phys. 59, 656 (1986)
42. M. Kuriyama, B. Steiner, R. C. Dobbryn, U. Laor, D. Larson, and M. Brown, submitted for publication, June 1988
43. T. Kitano, T. Ishikawa, and J. Matsui, Jap. J. Appl. Phys. 25, L282 (1986)
44. T. Kitano, J. Matsui, and T. Ishikawa, Jap. J. Appl. Phys. 24, L948 (1985)
45. J. Matsui, T. Kitano, T. Kamejima and T. Ishikawa, GaAs and Related Compounds, Biarritz, Inst. Phys. Conf. 74, 101 (1984)
46. T. Kitano, H. Ono, and J. Matsui, Jap. J. Appl. Phys. 25, L761 (1986)
47. B. Steiner, M. Kuriyama, R. C. Dobbryn, and U. Laor, J. Research, NBS in press (1988)
48. M. Kuriyama, in "Advanced Techniques for Microstructure Characterization", T. R. Anatharaman and R. Krishnan, eds, in press (1988)
49. B. Steiner, U. Laor, M. Kuriyama, and R. C. Dobbryn, J. Crystal Growth, 87, 79 (1988)
50. R. Spal, R. C. Dobbryn, H. E. Burdette, G. G. Long, W. J. Boettinger, and M. Kuriyama, Nucl. Inst. Methods 222, 189 (1984)
51. W. J. Boettinger, H. E. Burdette, E. N. Farabaugh, and M. Kuriyama, in "Advances in X-Ray Analysis" 20, 207 (1977)
52. D. B. Holt, J. Phys. Chem. Solids 30, 1297 (1969)
53. A. S. Jordan, A. R. Von Neida, and R. Caruso, J. Crystal Growth 70, 555 (1984)
54. S. Tohno, S. Shinoyama, A. Yamamoto, and C. Uemura, J. Appl. Phys 54, 666 (1983)
55. D. B. Holt, M. I. Abdalla, F. H. Gejji, and D. M. Wilcox, Thin Solid Films 37, 91 (1976)
56. K. Wada and N. Inoue, Appl. Phys. Lett. 47, 945 (1985)

57. J. Lagowski, D. G. Lin, T.-P. Chen, M. Skowronski, and H. C. Gatos, Appl. Phys. Lett. 47, 929 (1985)
58. T. Kikuta, K. Terashima, and K. Ishida, Jap. J. Appl. Phys. 22, L541 (1983)
59. E. R. Weber, H. Ennen, U. Kaufmann, J. Windscheif, and J. Schneider, J. Appl. Phys. 53, 6140 (1982)
60. J. Lagowski, H. C. Gatos, J. M. Parsey, K. Wada, M. Kaminska, and W. Walukiewicz, Appl. Phys. Lett. 40, 342 (1982)
61. D. E. Holmes, K. R. Elliott, R. T. Chen, and C. G. Kirkpatrick, Semi-Insulating III-V Materials Evian, 19 (1982)
62. L. B. Ta, H. M. Hobgood, A. Rohatgi, and R. N. Thomas, J. Appl. Phys. 53, 5771 (1982)
63. D. E. Holmes, R. T. Chen, K. R. Elliott, and C. G. Kirkpatrick, Appl. Phys. Lett. 40, 46 (1982)
64. T. S. Plaskett, J. M. Woodall, and A. Sebmüller, J. Electrochem. Soc. 118, 115 (1971)
65. D. J. Chadi, J. Vac. Sci. Technol. A5, 834 (1987)
66. M. D. Pashley, K. W. Haberern, W. Friday, J. M. Woodall, and P. D. Kirchner, Phys. Rev. Lett. 60, 2176 (1988)



ORIGINAL PAGE IS
OF POOR QUALITY



Fig 2

200m

100

ORIGINAL PAGE IS
OF POOR QUALITY



010

10

Fig 3

1 mm

ORIGINAL PAGE IS
OF POOR QUALITY



ORIGINAL PAGE IS
OF POOR QUALITY

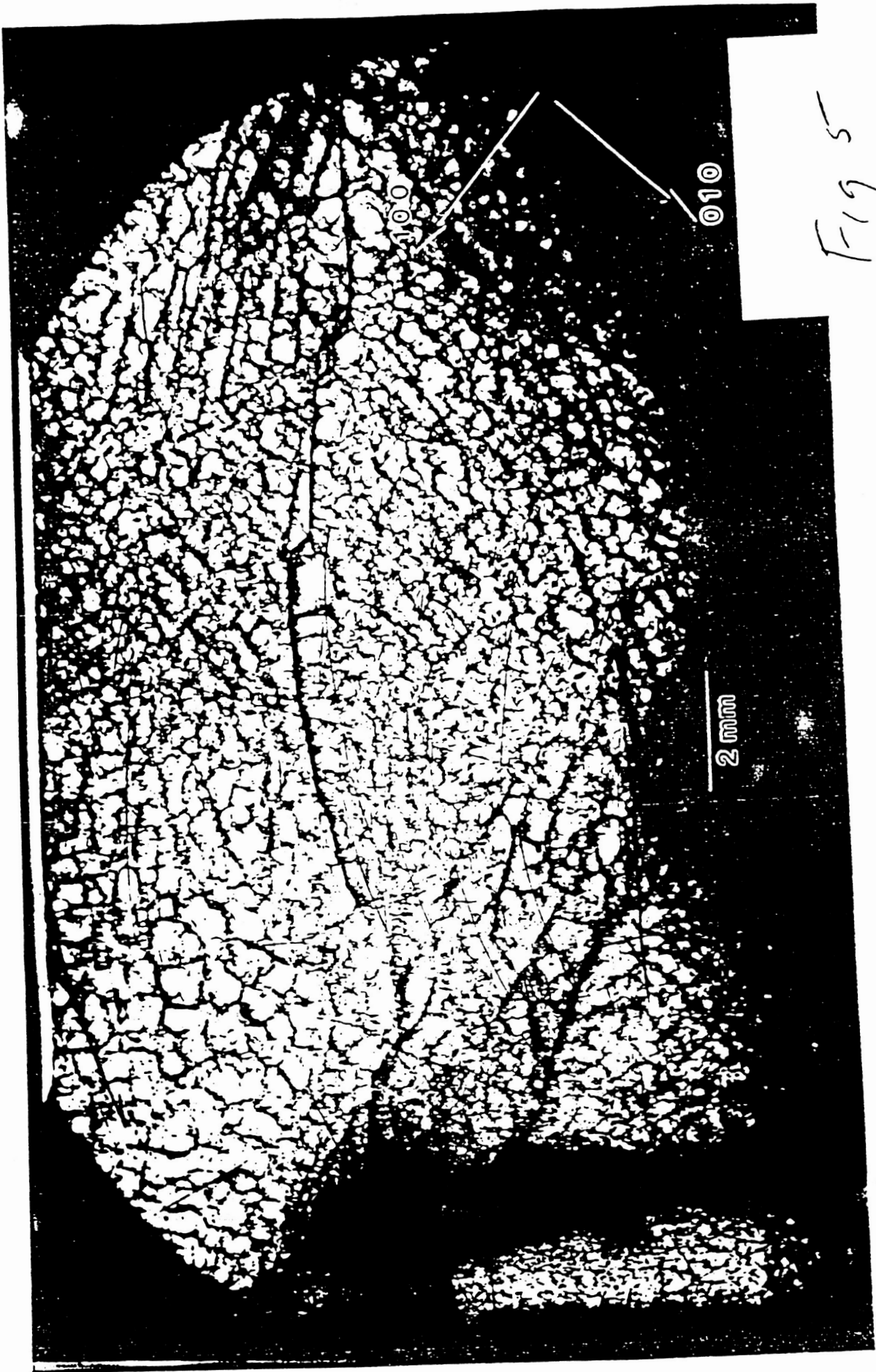


Fig 5

ORIGINAL PAGE IS
OF POOR QUALITY

ORIGINAL PAGE IS
OF POOR QUALITY

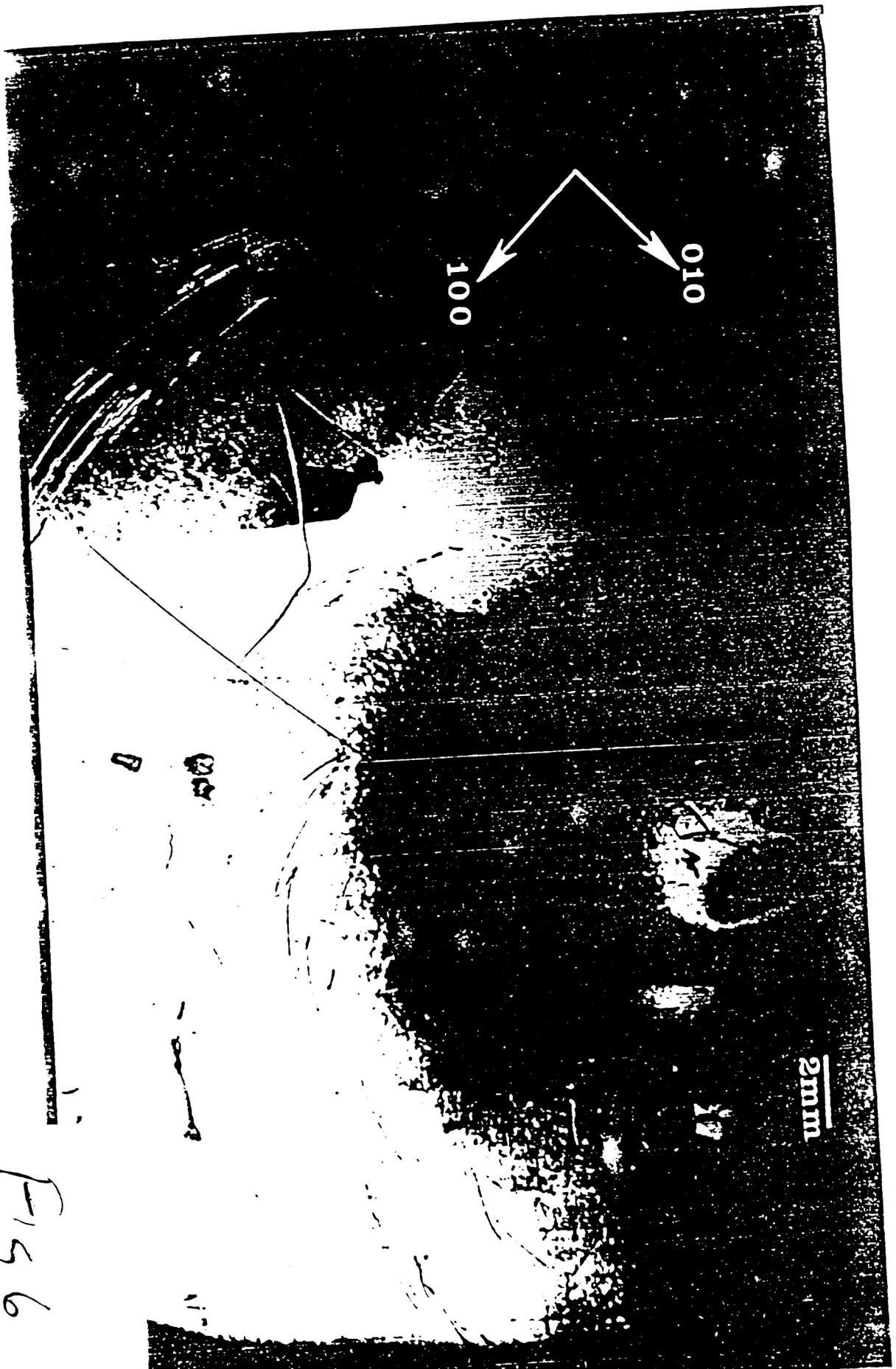
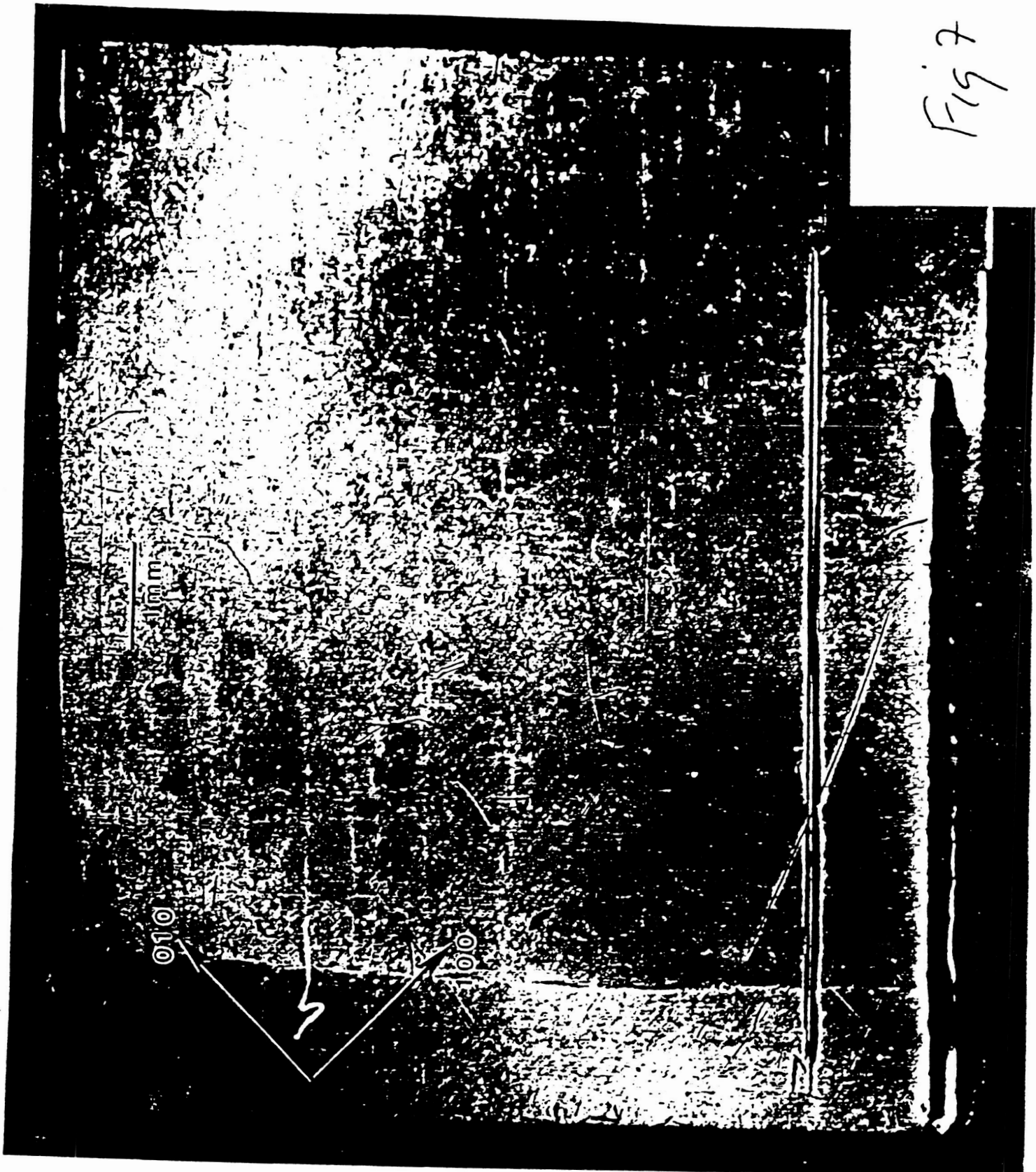
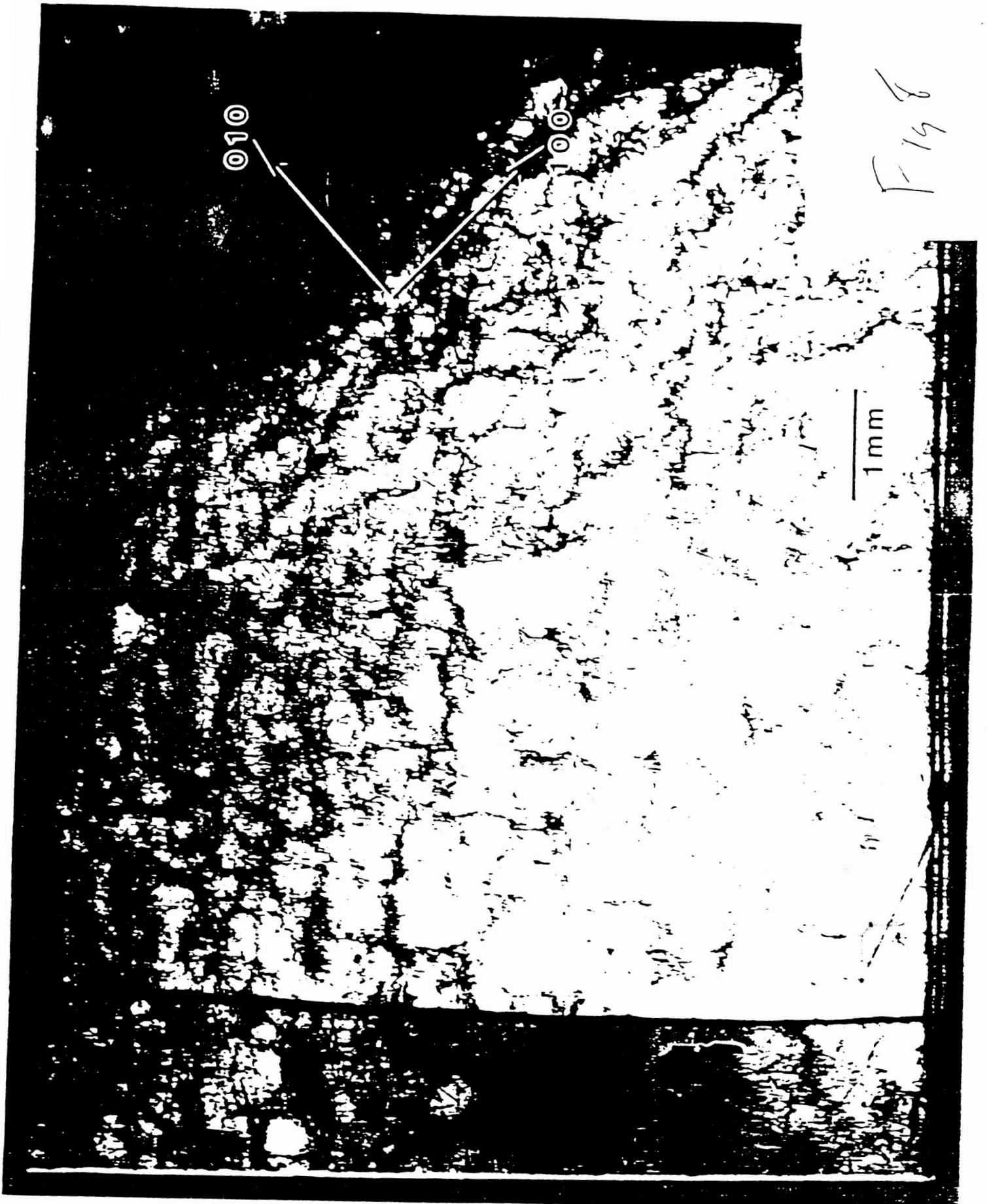


Fig 6

Fig 7



ORIGINAL PAGE IS
OF POOR QUALITY

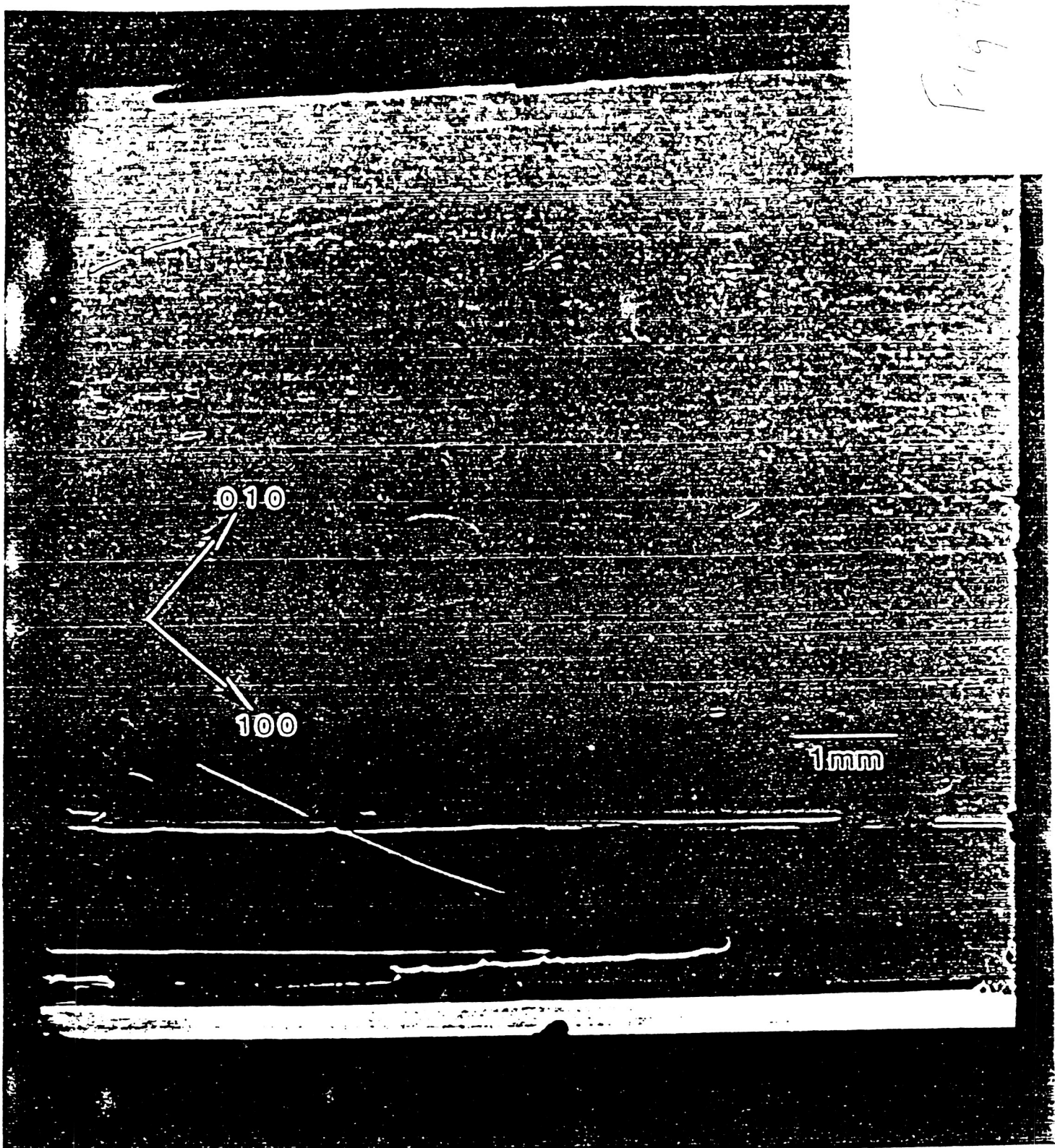


F148

ORIGINAL PAGE IS
OF POOR QUALITY

ORIGINAL PAGE IS
OF POOR QUALITY

Fig 4

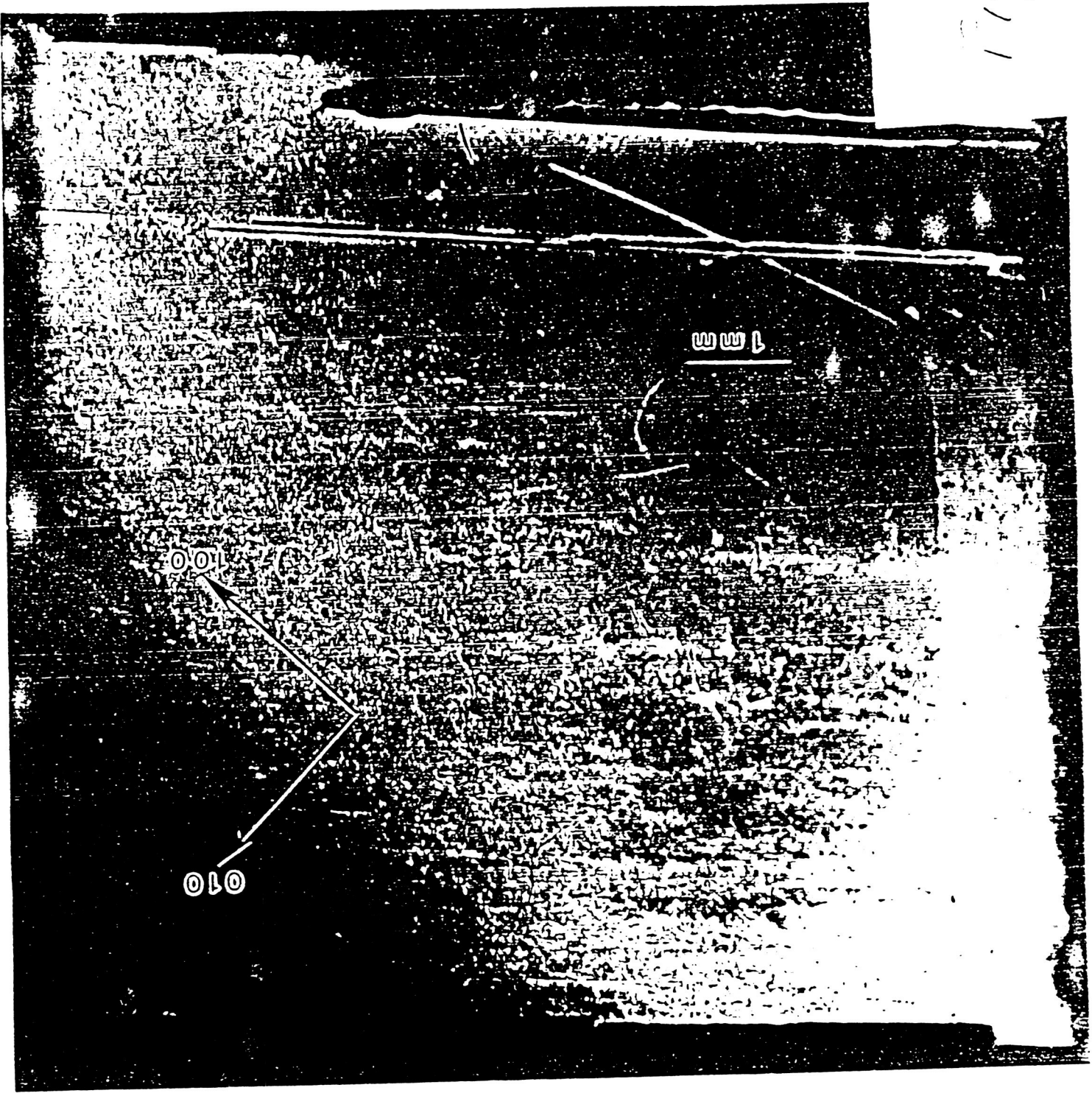


010

100

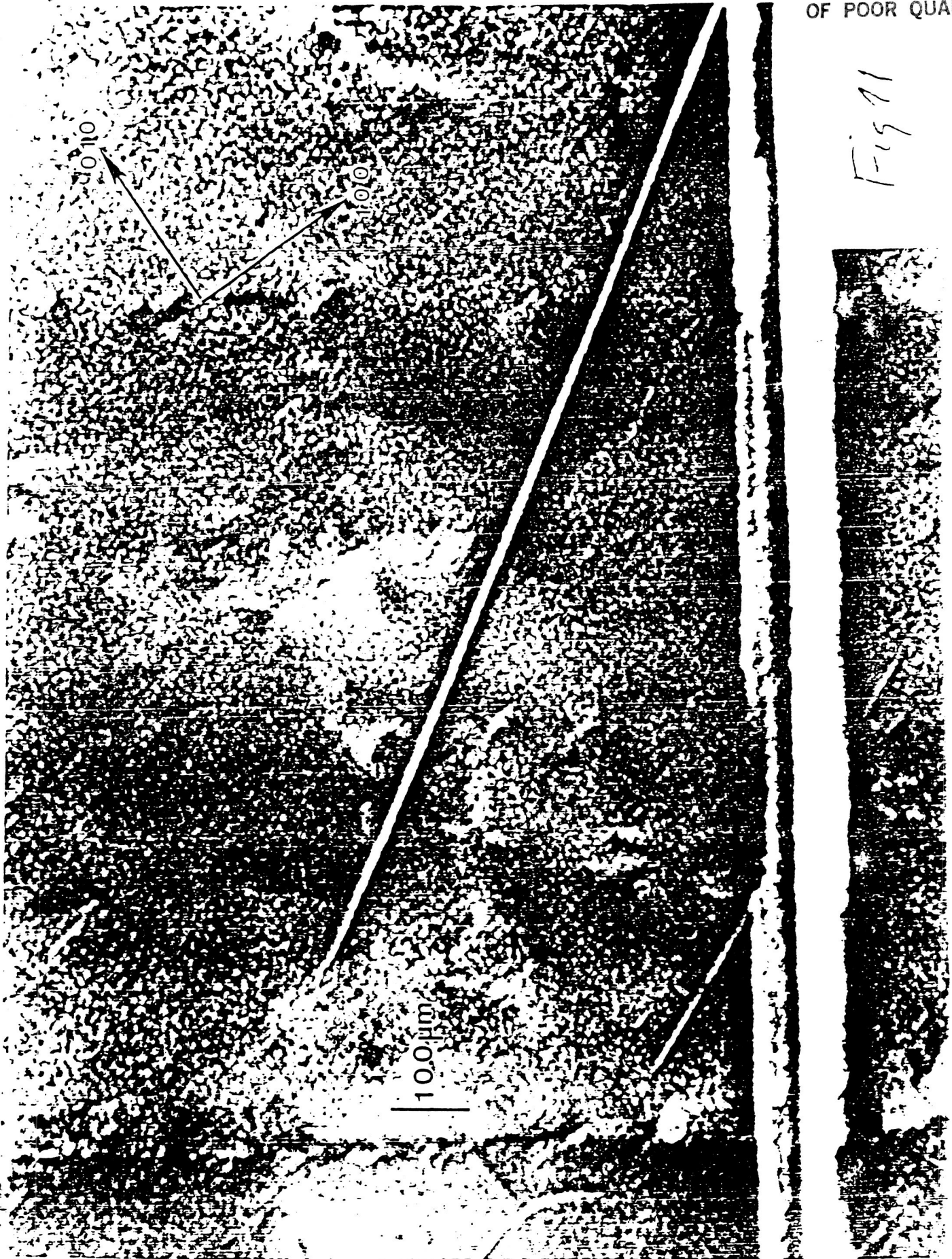
1mm

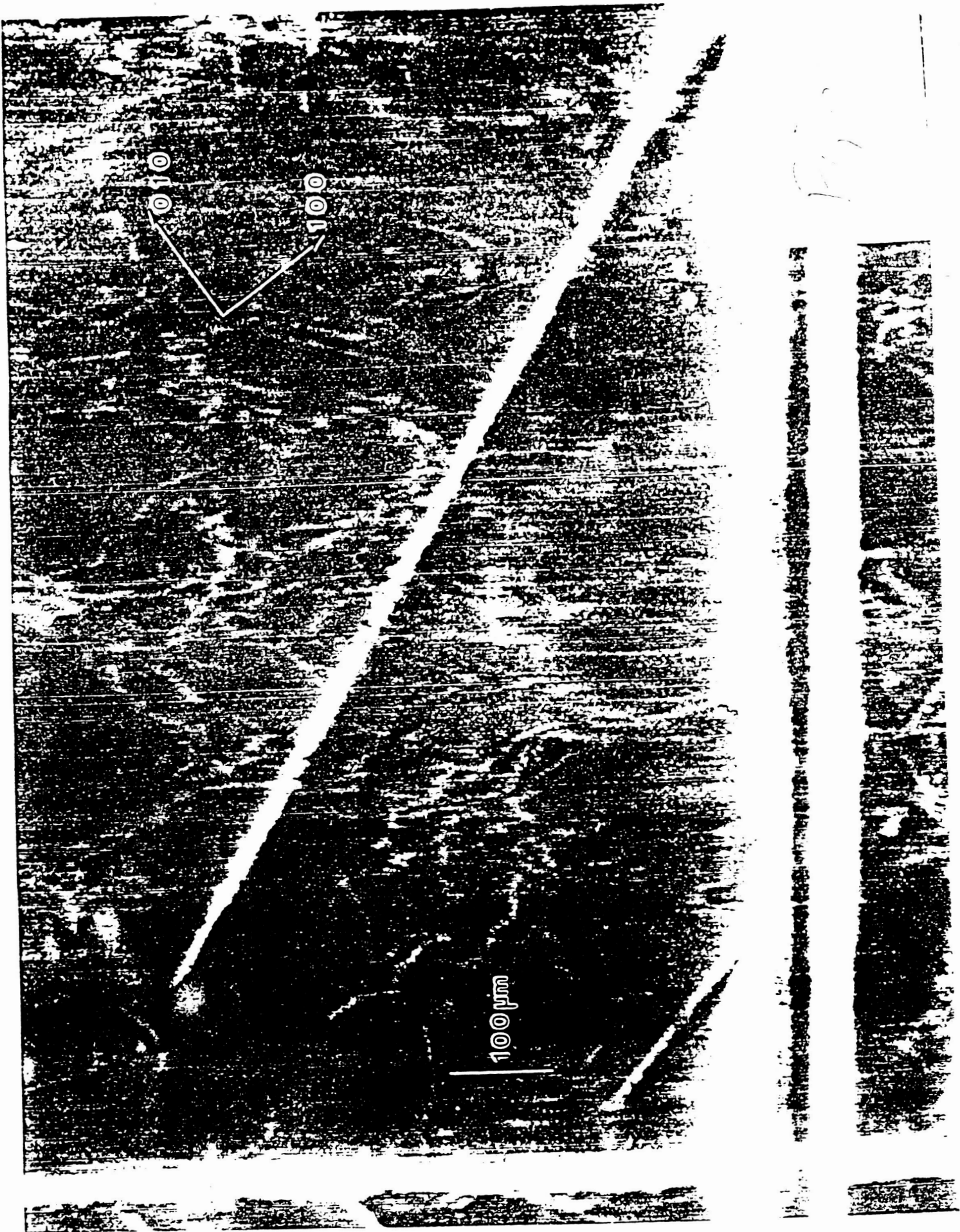
119 10



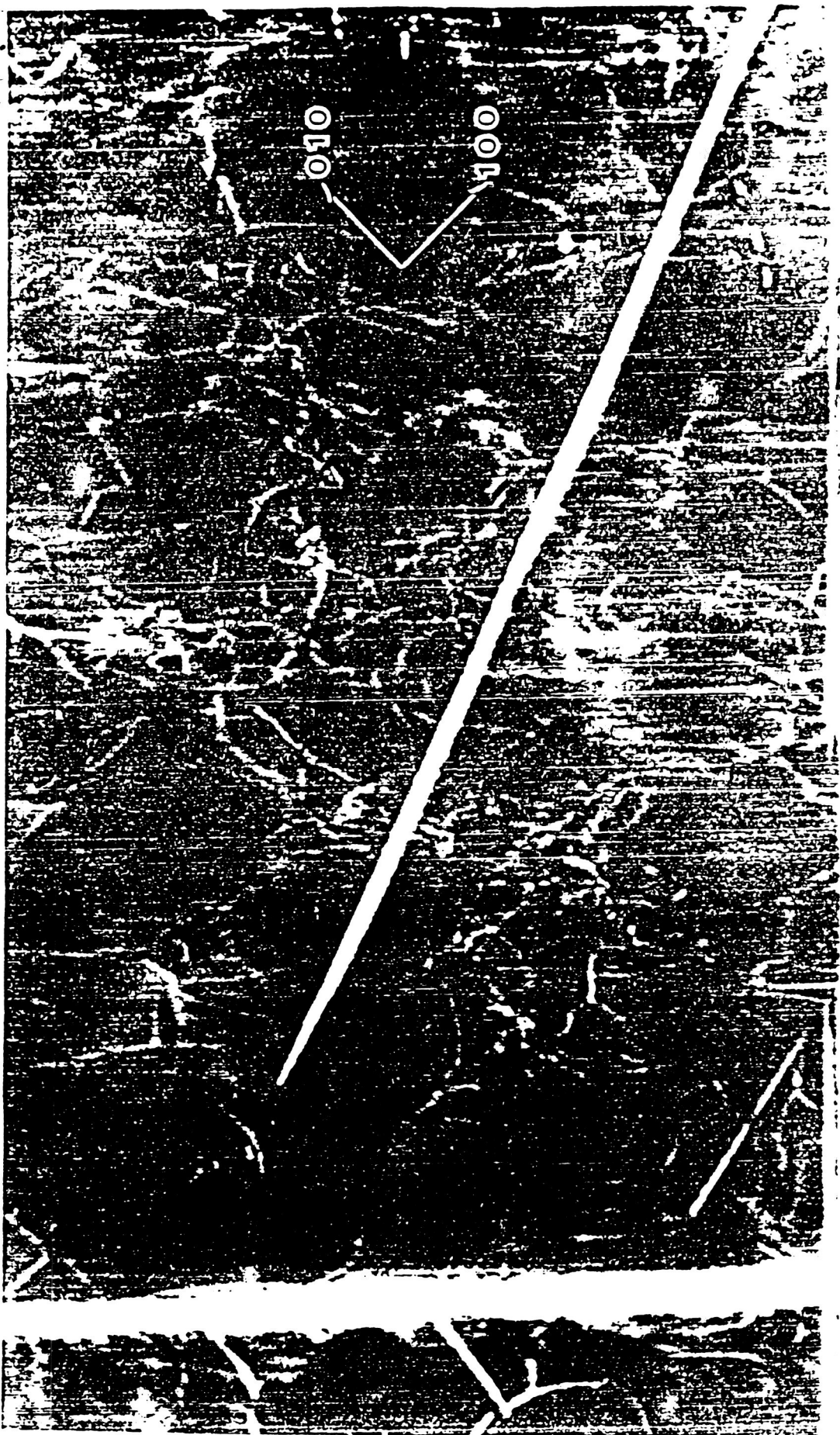
ORIGINAL PAGE IS
OF POOR QUALITY

Fig 11





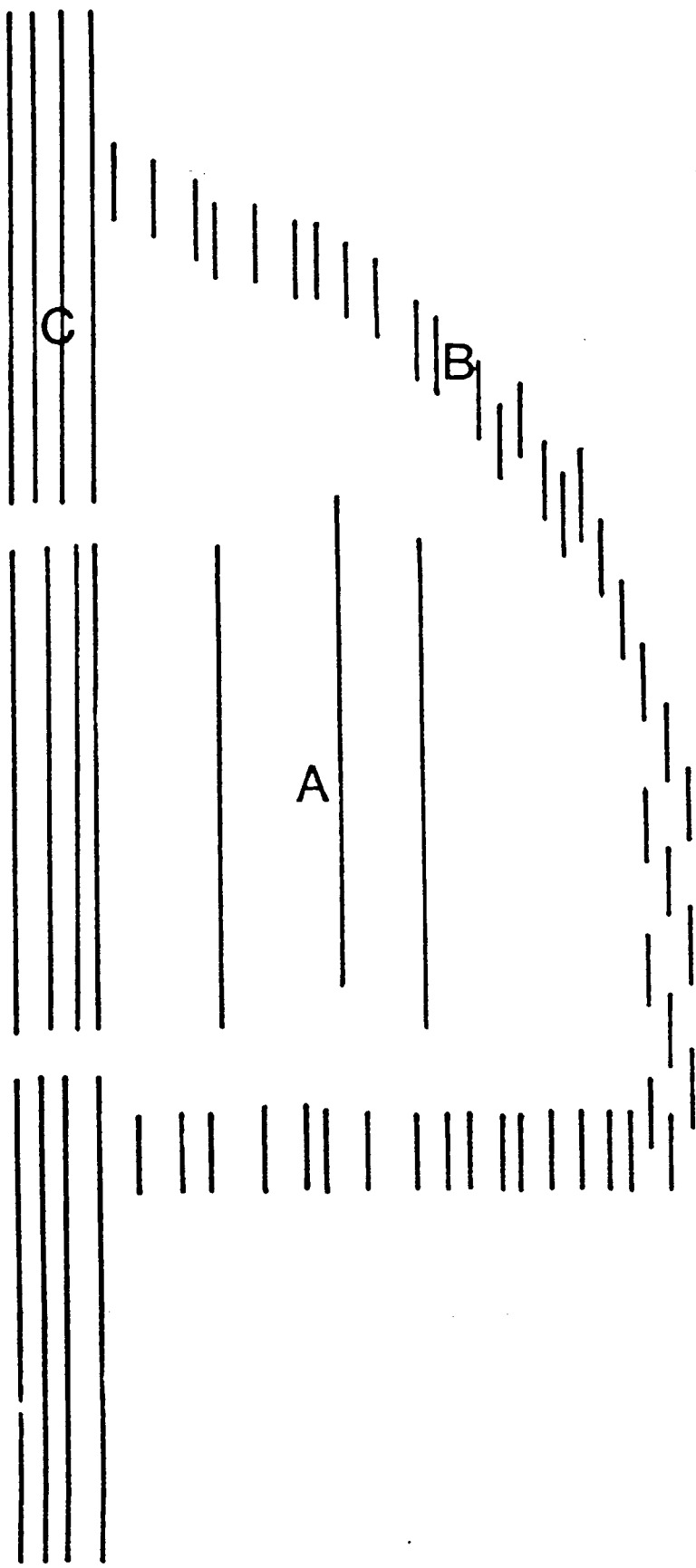
ORIGINAL PAGE IS
OF POOR QUALITY



100 μm

Fig 13

ORIGINAL PAGE IS
OF POOR QUALITY



50 μ m

Fig 14



[0 1 0]

[1 0 0]

$\rightarrow | \leftarrow a/\sqrt{2} = \text{lattice constant}$

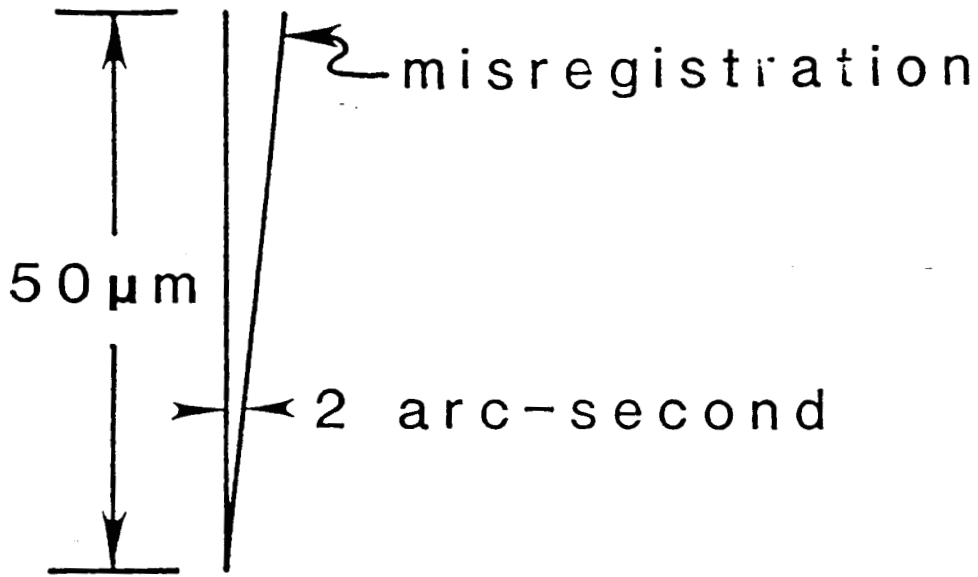
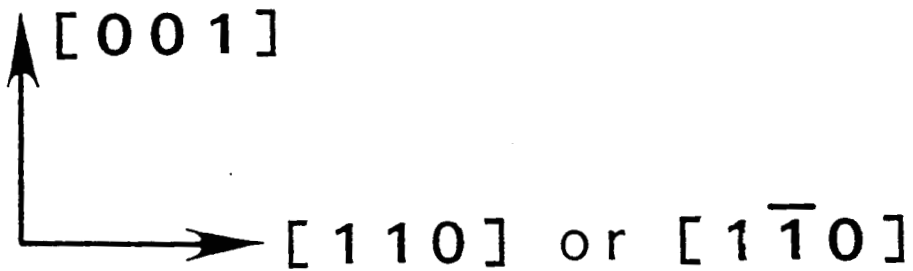
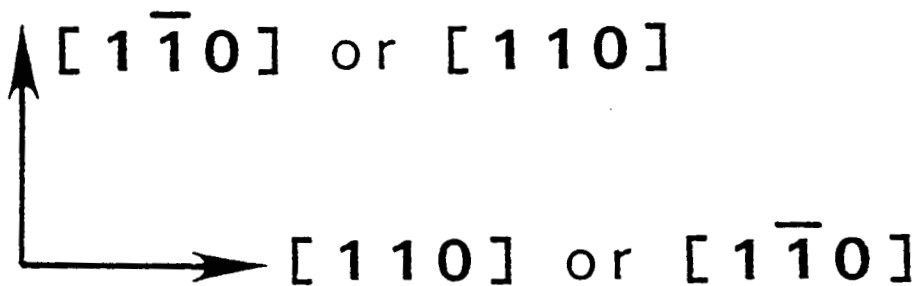


Fig 15

Type A & C platelet orientation



Type B platelet orientation



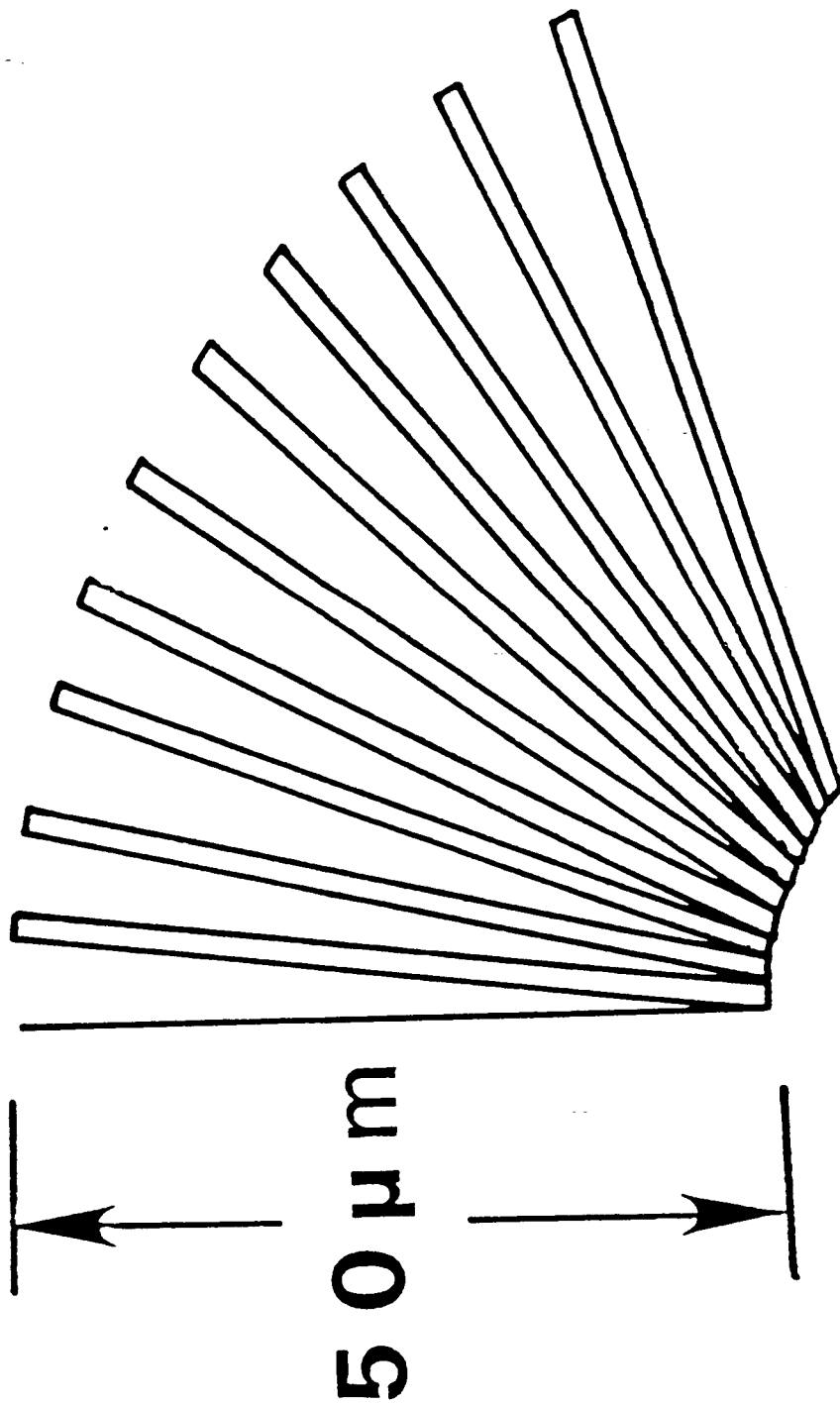


Figure 4